High Performance Electrocatalytic Reaction of Hydrogen and Oxygen on Ruthenium Nanoclusters

Ruquan Ye,[†] Yuanyue Liu,[€] Zhiwei Peng,[†] Tuo Wang,[†] Almaz S. Jalilov,[†] Boris I. Yakobson,[†,‡,§,] Su-Huai Wei[€,1] and James M. Tour[†,‡,§,*]*

[†]Department of Chemistry, [‡]Smalley Institute for Nanoscale Science and Technology,

[§]Department of Materials Science and NanoEngineering,

Rice University, 6100 Main Street, Houston, Texas 77005, USA

[€]National Renewable Energy Laboratory, Golden, CO, USA, 80401

**Email: biy@rice.edu, tour@rice.edu*

Abstract The development of catalytic materials for the hydrogen oxidation, hydrogen evolution, oxygen reduction or oxygen evolution reactions with high reaction rates and low overpotentials are key goals for the development of renewable energy. We report here Ru(0) nanoclusters supported on nitrogen-doped graphene as high-performance multi-functional catalysts for the hydrogen evolution reaction (HER) and oxygen reduction reaction (ORR), showing activities similar to that of commercial Pt/C in alkaline solution. For HER performance in alkaline media, sample Ru/NG-750 reaches 10 mA cm^{-2} at an overpotential of 8 mV with a Tafel slope of 30 mV $decade^{-1}$. The high HER performance in alkaline solution is advantageous because most catalysts for ORR and oxygen evolution reaction (OER) also prefer alkaline solution environment whereas

[1] Present address: Beijing Computational Science Research Center, Beijing 100193, China

degrade in acidic electrolytes. For ORR performance, Ru/NG effectively catalyzes the conversion of O_2 into OH^- *via* a 4 *e* process at a current density comparable to that of Pt/C. The unusual catalytic activities of Ru(0) nanoclusters reported here are important discoveries for the advancement of renewable energy conversion reactions.

Keywords hydrogen evolution reaction, hydrogen oxidation reaction, oxygen reduction reaction, ruthenium, electrocatalyst

Introduction

Hydrogen, an excellent energy carrier, has attracted tremendous research effort due to its theoretical highest mass energy density (120 MJ kg^{-1}) and environmentally friendly nature.[1] Development of an effective and efficient catalyst to generate hydrogen by electrochemical or solar-energy-driven water splitting is critical to the development of hydrogen as a vehicular energy source. The capital costs of H_2 production by water electrolysis is \$4.20/ggea in 2011 and in a target of \$2.30/ggea in 2020 as released by the US Department of Energy.[2] Water splitting is comprised of two half reactions: hydrogen evolution ($2H^+ + 2e \rightarrow H_2$) and oxygen evolution ($4OH^- + 4h \rightarrow 2H_2O + O_2$). Besides the intrinsic catalytic activity of the materials in the two half reactions, one of the obstacles slowing the development of the hydrogen economy is the incompatibility of the anodic and cathodic catalysts in the same electrolyte environment, which results in additional cost and concerns in device fabrication, such as corrosion issues and use of an expensive membrane separator. For instance, MoS_2 and MoP are electrocatalytically active in hydrogen evolution under acidic conditions, yet the electrocatalytic activity drops gradually under alkaline conditions.[3-5] On the other hand, metal oxides and layered double hydroxides (LDHs), such as CoO_x, MnO_x, and Ni-Fe-LDH, are electrochemically active for oxygen evolution under alkaline conditions, whereas these materials become inactive when used in acidic conditions, particularly due to the dissolution of active sites.[6-9] Therefore, development of an active catalyst for hydrogen evolution under alkaline conditions would be advantageous to mitigate acid corrosion, while affording cathodic and anodic catalyst compatibility.

Platinum (Pt), a major precious metal commodity, has remarkable catalytic activity in the hydrogen reduction reaction. Tremendous research effort has taken place to develop a substitute that possesses similar water reduction catalytic activity. For example, molecular biomimetics such as [Ni-Fe]- and [Fe] hydrogenases have been successfully synthesized with a reported turnover frequency (TOF) > 100000 s^{-1}.(ref [10,11]) However, these materials are usually not conductive, are oxygen-sensitive and require the use of sacrificial agents. They are not suitable for long-term electrocatalysis or for the large scale production of hydrogen. Other types of electrocatalysts, based on transition metal semiconductors such as MoS_2 and MoP, have been found to be active in water splitting. It is interesting to note that group-5 metal dichalcogenides (hexagonal phase of NbS_2 and TaS_2) have been recently discovered to possess higher performance over MoS_2 and WS_2 because of their surface activity, in contrast to MoS_2 and WS_2 that are only edge-active, as well as self-optimizing performance owing to the combination of surface activity and weak interlayer coupling.[12] Yet these materials either suffer from high onset overpotentials and Tafel slopes, or a low hydrogen turnover frequency when compared with Pt. (ref 3,13) In addition, they degrade in alkaline water. Moreover, unlike Pt that is active in both hydrogen reduction and oxygen reduction catalytic reactions, biomimetic molecular catalysts and transition metal semiconductors are usually active in one type of catalytic reaction, and they become inactive when used in other systems.

In this work, we report a high performance electrocatalyst based on crystalline ruthenium (Ru) nanoclusters supported on nitrogen-doped graphene (Ru/NG) for both hydrogen evolution and oxygen reduction. For hydrogen evolution, the catalyst reaches an onset potential of ~ 0 V in both acidic and alkaline water with a Tafel slope of 44 and 30 mV $decade^{-1}$, respectively. The overpotentials required to deliver a current density of 10 mA cm^{-2} and 20 mA cm^{-2} in alkaline

media are 8 mV and 14 mV, respectively. To our knowledge, this is the highest performing electrocatalyst for hydrogen evolution from aqueous solutions. In addition, the Ru nanoclusters are electrocatalytically active in converting O_2 into HO^-, making it also suitable for oxygen reduction fuel cell applications.

Result and discussion

The Ru/NG was prepared in two steps. As shown in Scheme 1, the first step is the nucleation of Ru(III) nanoclusters on graphene oxide (GO) by hydrolysis of $Ru(NH_3)_6Cl_3$ in GO aqueous solution at 160 °C. The use of graphene as a substrate is known to be advantageous in terms of its large surface area[14], high conductivity[15,16] and synergistically enhanced performance.[17-19] To avoid the aggregation of Ru (III) nanoclusters and coagulation effect due to electrostatic interactions between GO and $Ru(NH_3)_6^{3+}$, the Ru content used was as low as 1.5 wt%. In the second step, Ru(III) nanoclusters were reduced in an NH_3/Ar environment at varying temperatures from 350 to 850 °C, which leads to the reduction of Ru(III) nanoclusters to Ru(0) nanoclusters, and GO to nitrogen-doped graphene (NG) (see Supporting Methods for details). The samples are termed as Ru/NG-x, where x signifies the synthetic temperature.

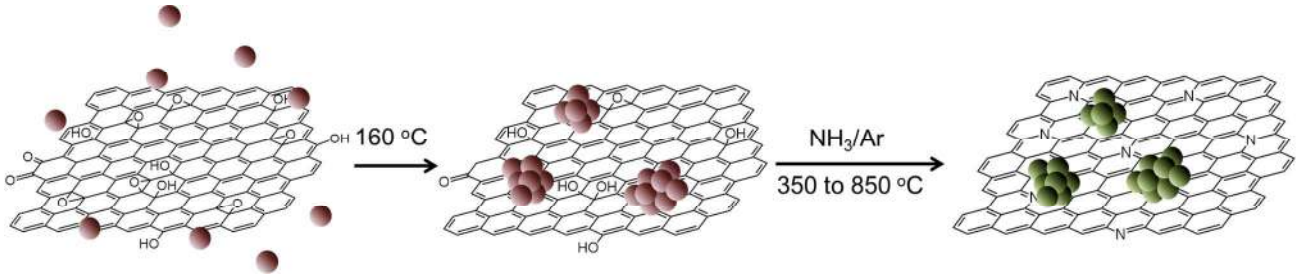

Scheme 1. Schematic illustration for the formation of Ru/NG. The first step is the nucleation of Ru(III) nanoclusters by mixing of $Ru(NH_3)_6Cl_3$ in GO solution. After that, Ru(III) is reduced

to Ru(0) in NH_3/Ar mixed gas at varying temperature from 350 to 850 °C, which also converts the GO to conductive N-doped graphene.

The morphology of Ru/NG was characterized by scanning electron microscopy (SEM) and transmission electron microscopy (TEM). Figure 1a-c reveals the porous structure of Ru/NG. In micrometer scale, Ru/NG prepared at different temperature show similar macroporous structure to each other. The TEM image (Figure 1d-f) shows that the Ru(0) nanoclusters are well distributed on NG. The average size distribution increases from 3.5 ± 1.3 nm for Ru/NG-450 to 5.8 ± 1.5 nm for Ru/NG-750 and 6.1 ± 1.1 nm for Ru/NG-850. The crystal structure of Ru/NG is further analyzed by X-ray diffraction (XRD). As shown in Figure 2a, the peaks at ~ 38°, ~ 41° and ~ 42° corresponding to (100), (002) and (101) facets of crystalline Ru(0), become more prominent as the temperature elevates, indicating higher temperature is in favor of forming crystalline Ru. X-ray photoelectron spectroscopy (XPS) also reveals the chemical state of Ru. The binding energy of Ru3d5/2 at ~ 280 eV becomes lower at higher temperature (Figure 2b), which indicates reducing at higher temperature favors a lower oxidation state of Ru. As to N1s XPS spectrum (Figure S1), the peak position shifts from 399.8 eV to 398.4 eV as the synthetic temperature raises from 350 °C to 550 °C, suggesting a transition of pyridonic and pyrrolic nitrogen to pyridinic nitrogen.[20] However, further increasing the temperature from 550 °C to 850 °C does not significantly alter the chemical environment of nitrogen. The atomic chemical compositions of Ru/NG are summarized in Table S1. It is noticeable that the atomic compositions percentages of Ru/NG-350 to Ru/NG-750 are similar to each other, and the nitrogen content increases slightly as the synthetic temperature rises to 750 °C. At 850 °C, due to the etching effect of NH_3, the carbon content drops significantly to 86%. The surface area of

Ru/NG is assessed by Brunauer–Emmett–Teller (BET) surface analysis (Figure 2c, d). The BET surface calculated from the adsorption and desorption curves (Figure 2c) reveal a surface area of 30.1, 266, 401.8, 379, 782 and 122 $m^2 g^{-1}$ for Ru/NG synthesized at 350, 450, 550, 650, 750 and 850 °C, respectively. Pore size distribution calculated differential nonlocal density functional theory (NLDFT) method (Figure 2d) shows that increasing the synthesis temperature from 350 to 750 °C results in an increasing abundance of micropores and mesopores volume. However, further increasing the temperature from 750 °C to 850 °C leads to a great loss of micropores and mesopores. The low surface area and the loss of micro- and mesopores for Ru/NG-850 are attributed to the over-etching of NH_3 at high temperature, as evidenced by the low carbon content at 850 °C (Table S1).

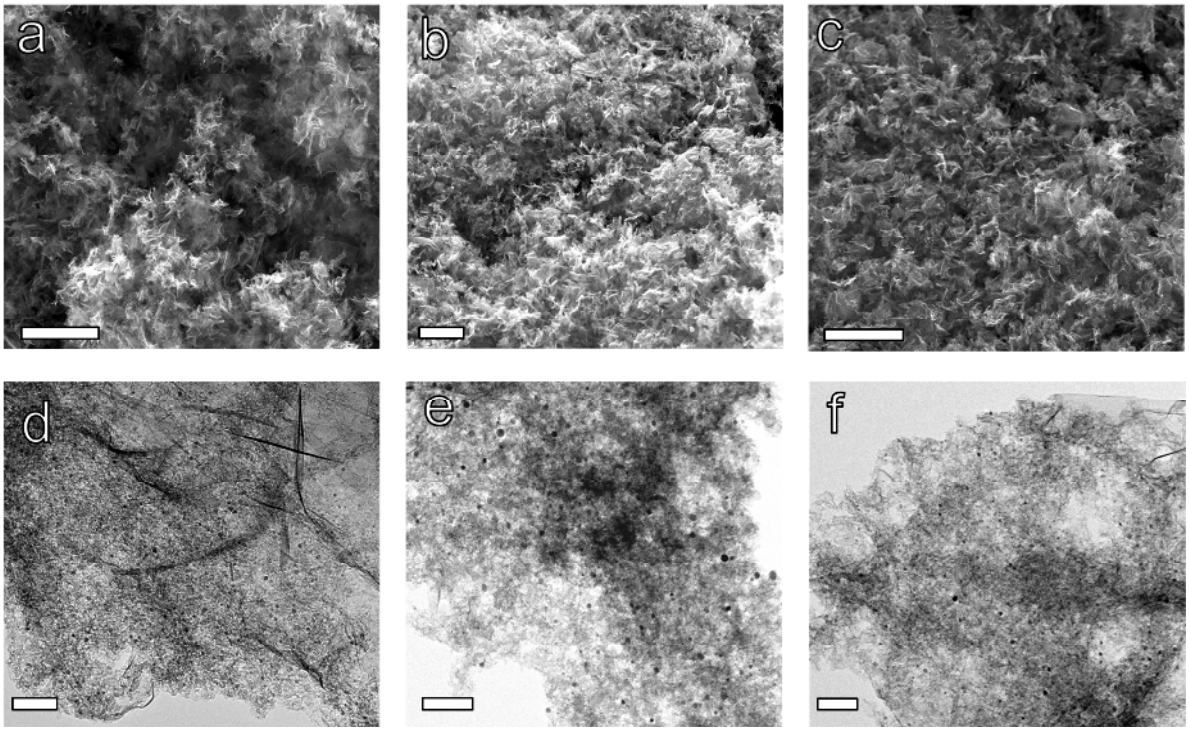

Figure 1. Morphology of Ru/NG. SEM image showing the porous structure of (a) Ru/NG-450, (b) Ru/NG-750 and (c) Ru/NG-850; scale bars are 25 μm. TEM image of (d) Ru/NG-450 and (e)

Ru/NG-750 and (f) Ru/NG-850 with uniform size distribution of Ru nanoclusters on NG; scale bars are 100 nm.

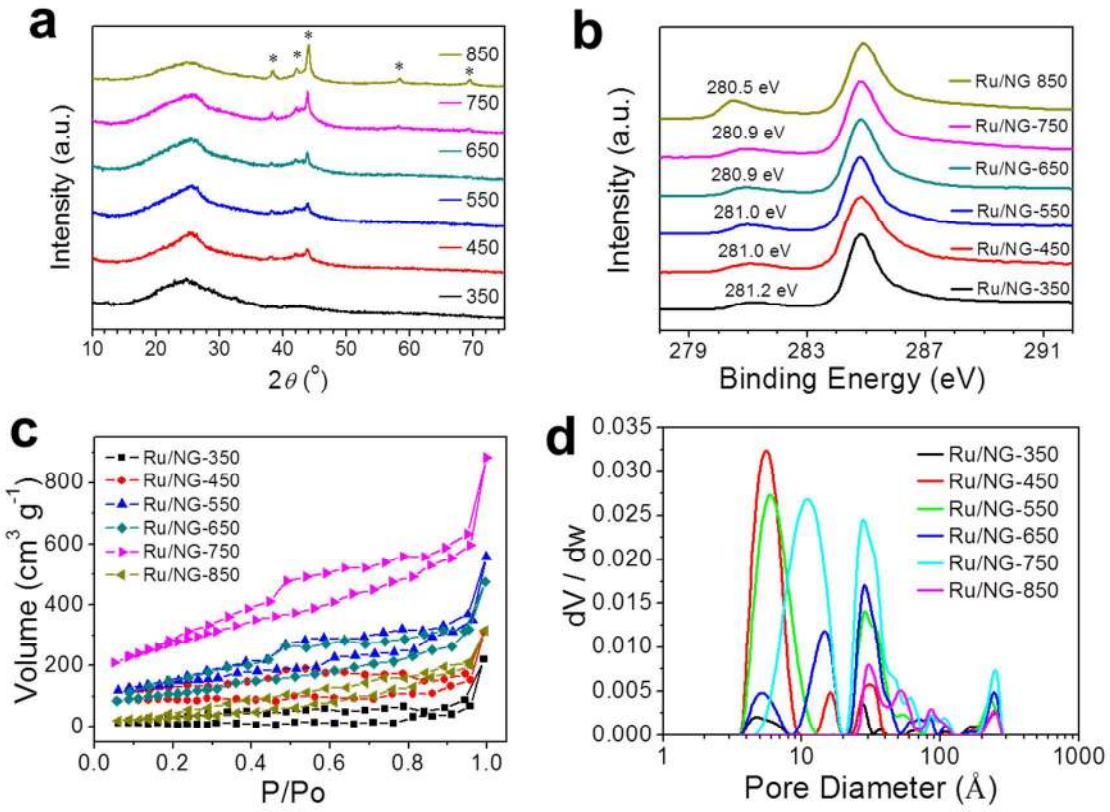

Figure 2. Structure characterization of Ru/NG synthesized at varying temperatures. (a) XRD, The crystalline facets of Ru(0) are marked with asterisks. (b) High resolution C1s and Ru3d5/2 XPS, (c) BET absorption and desorption curves and (d) Pore size distribution calculated by differential nonlocal density functional theory (NLDFT) method from (c).

The catalytic activity of Ru/NG in HER was assessed using a three-electrode electrochemical cell in both 1 M KOH and 0.5 M H_2SO_4 solutions. Figure 3a and S2 display linear sweep voltammetry (LSV) polarization curves (iR compensated) of Ru/NG in 1 M KOH and 0.5 M H_2SO_4 solution and their performances are summarized in Figure S3. In both acidic

and alkaline media, the HER onset potential of Ru/NG-750 approaches ~ 0 V, which is the same as that of Pt/C and indicates the sample exhibits a high catalytic activity. However, at lower or higher synthetic temperature, the HER onset potential of Ru/NG becomes higher. The current density of Ru/NG-750 reaches 10 mA cm^{-2} at overpotentials of 8 mV and 53 mV in alkaline and acidic water, respectively. The HER mechanism of Ru/NG is studied by Tafel slope shown in Figure 3b. As summarized in Figure S3, the Tafel slopes of Ru/NG-750 decrease to as low as 30 mV dec^{-1} and 44 mV dec^{-1} in alkaline and acidic water, respectively. This suggests that Ru/NG-750 primarily goes through a Volmer–Heyrovsky HER mechanism with the Heyrovsky reaction as the rate determining step (RDS) in alkaline water, and aided with a $Volmer_{(RDS)}$–Tafel HER mechanism in acidic water.[13,21,22] The performance of Ru/NG has outperformed the reported data with even higher mass loadings. For example, MoS_2–based catalysts usually require > 150 mV overpotential to produce 10 mA cm^{-2} current at a mass loading of 200 to 300 μg cm^{-2}, primarily because these materials have a high onset potential at ~ 110 mV.[5,13,21] Metal phosphide/phosphosulfide can attain a current density of 10 mA cm^{-2} at ~ 80 mV overpotential at a higher mass loading of 1 to 3 mg cm^{-2}. These materials have lower onset potential at ~ 50 mV overpotential, whereas a higher mass loading is required to reduce the overpotential due to a higher Tafel slope.[3,4,23,24] Nonetheless, Ru/NG-750 shares both the advantages of low onset overpotential and small Tafel slope. It is noteworthy that Ru only accounts for 0.6 at% of the sample (Table S1).

To further assess the intrinsic catalytic activities, the hydrogen turnover frequency (TOF), which evaluates the number of H_2 molecules generated per second per active site, was investigated in comparison to reported catalysts. The electrochemical active surface area (ECSA) of Ru/NG was estimated from the capacitive currents at different scan rates in a manner similar

to that disclosed in the literature (see Figures S5-8 and Supporting Equations for details).[3,23,24] Copper stripping for measurement of ECSA is not applicable here, particularly due to the dissolution of Ru in acidic electrolyte and precipitation of Cu^{2+} in alkaline electrolyte.[25] The ECSA of Ru/NG and Pt/C reported here are overestimated, since both the substrate and Ru/Pt contribute to the capacitive currents, whereas the carbon substrate has little HER activity. Therefore, the TOFs of Ru/NG and Pt/C are only conservative estimates. As shown in Figure 3c, the TOF values of Ru/NG in 1 M KOH is displayed along with Pt/C and reported data $MoS_xP_{2(1-x)}$,(ref 26) CoP,(ref 24) Ni_2P,(ref 23) and $[Mo_3S_{13}]^{2-}$ (ref 13) collected in 0.5 M H_2SO_4. The TOF values in acid are also measured (Figure S2c), whereas due to Ru dissolution issues, there might be systematic errors that are not discussed in detail here. As depicted in Figure 3c, Ru/NG-750 reaches a TOF value of 0.35 $H_2\ s^{-1}$ in 1 M KOH at 100 mV overpotential, which is higher than that of Pt/C in the same media. This performance has surpassed those of transition metal dichalcogenides in acidic media as displayed in Figure 3c. The electrocatalytic stability of Ru/NG is examined in 1 M KOH and 0.5 M H_2SO_4 solution with continuous cycling at a scan rate of 100 mV s-1. Ru/NG exhibits excellent HER catalytic stability in alkaline water. As shown in Figure 3d, no apparent shift was observed for Ru/NG-850 after 4000 continuous LSV cycles between -0.3 and 0.1 V in 1 M KOH solution. A slight increase in overpotential for Ru/NG-750 is observed after 4000 cycles, which is attributed to the detachment of materials from the electrode due to the high hydrogen evolution rate instead of from degradation of performance. However, both Ru/NG-750 and Ru/NG-850 display a significant inferior HER activity after 500 cycles in 0.5 M H_2SO_4. The TEM image of Ru/NG-850 after cycling (Figure S4a,b) reveals a graphene surface with fewer nanoparticles present when compared to the as-prepared sample (Figure 1f) and the Ru3d5/2 XPS intensity declines (Figure 4c) after cycling, indicating the

dissolution of Ru in acid media. High resolution Ru3d5/2 XPS surface analysis (Figure S4c) shows that the binding energy of Ru3d5/2 shifts from 280.9 eV to 280.4 eV and 280.6 eV in alkaline and acid media after cycling, respectively, suggesting an *in situ* reduction of Ru on HER cycling.

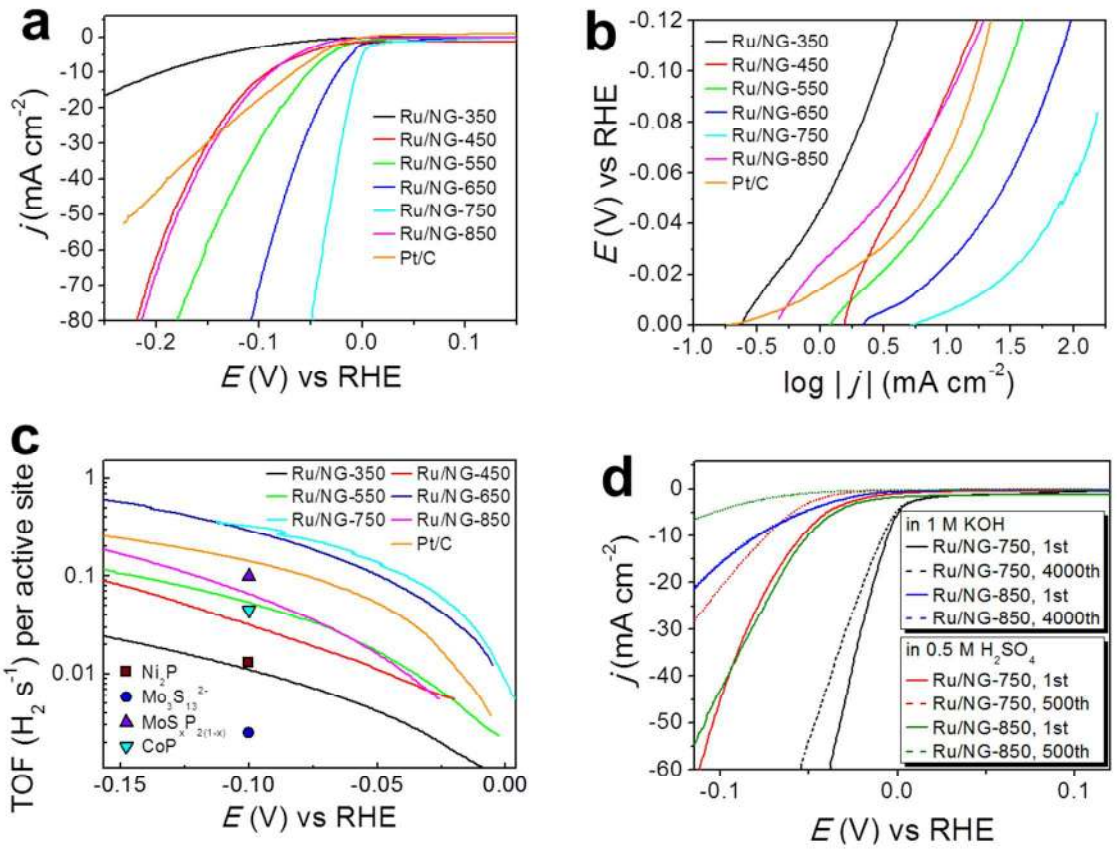

Figure 3. HER activity of Ru/NG at varying temperatures in 1 M KOH solution. (a) LSV polarization curves (iR compensated) of Ru/NG and Pt/C in 1 M KOH solution at scan rate of 5 mV s^{-1}. (b) Tafel slopes of Pt/C and Ru/NG derived from (a). (c) TOF of Ru/NG and Pt/C in base calculated using 40 μF cm^{-2} as the specific capacitance standard. Data for $MoS_xP_{2(1-x)}$ (ref 26), CoP (ref 24), Ni_2P (ref 23) and $[Mo_3S_{13}]^{2-}$ (ref 13) in 0.5 M H_2SO_4 are displayed for comparison. (d) Stability of Ru/NG-750 and Ru/NG-850 in 1 M KOH and 0.5 M H_2SO_4. It is noticeable that

some part of Ru/NG-750 substrate falls off during the cycling test in 1 M KOH due to the high hydrogen evolution rate.

Nitrogen-doping plays an important role in improving the electrocatalytic performance of Ru/NG. As shown in Figure S9a, the sample without nitrogen doping, Ru/G-750, displays a higher overpotential (~ 35 mV) to reach a current density of 10 mA cm^{-2} *vs* 10 mV for Ru/NG-750. In contrast, as shown in the inset of Figure S9a, both the HER onset overpotentials of Ru/NG-750 and Ru/G-750 are at ~ 0 V. XRD data (Figure S9b) shows a similar crystalline signal of graphene and Ru(0) in both samples of Ru/NG-750 and Ru/G-750, whereas BET analysis (Figure S9c,d) reveals that Ru/NG-750 possesses a much higher surface area and a higher density of micro- and mesopores. The enlarged surface area and pore volume improve the catalytic performance of Ru/NG-750 over Ru/G-750. Besides the surface area, synergistic effects and stronger interactions between the Ru nanoclusters and NG might also contribute to the enhanced performance, as suggested from the literature where the catalytic activity of nanoparticles on NG is generally superior to that on G.[17,27-29]

The high-performance HER activity of Ru/NG-750 arises from the more highly crystalline Ru(0) nanoparticles and the high surface area of the carbon substrate. As analyzed by the XRD pattern (Figure 2a), Ru/NG-750 has the better crystalline Ru(0) nanoparticles, which correlates to the much lower Tafel slope and larger TOF value as compared to Ru/NG synthesized at lower temperature. Although the Ru(0) XRD intensity of Ru/NG-850 is the strongest, the HER performance suffers from low surface area (Figure 2c,d).

To further understand the intrinsic HER activity of crystalline Ru(0), we performed density-functional-theory (DFT) calculations using projector augmented wave (PAW)

pseudopotentials[30,31] and a Perdew–Burke–Ernzerhof (PBE) exchange-correlation functional[32] as implemented in Vienna *ab-initio* Simulation Package (VASP).[33,34] The H adsorption is modelled by using few layers of Ru with the bottom layer fixed in the direction perpendicular to the surface. The differential adsorption energy, which represents the energy benefit/cost to adsorb one H on catalyst and therefore reflects the kinetics of HER, is defined in eq 1:

$$G_{diff} = G[\text{metal}+n\text{H}] - G[\text{metal}+(n\text{-}1)\text{H}] - 1/2G(\text{H}_2) \quad (1)$$

where G[metal+nH] is the free energy of the catalyst with n H atoms adsorbed, and $G(H_2)$ is the free energy of an H_2 molecule. We find that G_{diff} = -0.08 eV for Pt, and -0.2 eV for Ru. According to Sabatiers' principle, the optimal G_{diff} at pH 0 should be close to zero.[35] Thus, Pt has a higher activity than Ru in acidic solution, in agreement with experiments. In alkaline solution, the HER is more likely limited by O-H bond cleavage of H_2O:[36,37] $H_2O^* + e \rightarrow H^* + OH^-(aq)$, where * denotes the species are adsorbed on the catalyst. Our calculations show that the Ru surface has a stronger binding with both H_2O and H than Pt by 0.17 and 0.11 eV, respectively. Here we use (111) surface as a representative example; DFT-D3 method[38] is used to correct the van der Waals part of the interaction between H_2O and metal. In other words, the free energies of the reactants and the products are shifted by approximately the same magnitude. According to the Bell–Evans–Polanyi principle, one can expect Ru and Pt to have similar reaction barriers. This explains their comparable HER performance in alkaline conditions.

Apart from the excellent HER activity, Ru/NG also possesses high activity in the oxygen reduction reaction (ORR). Figure 4a shows the CV curves in O_2-saturated 0.1 M KOH solutions. Similar to the HER activity, we find that the $E_{1/2}$ of oxygen reduction potential of Ru/NG shifts from 0.73 V to 0.83 V as the synthetic temperature raises from 350 °C to 850 °C, indicating a higher ORR activity at higher synthetic temperature. The ORR kinetics of Ru/NG in 0.1 M KOH

is further evaluated using a rotating-disk electrode (RDE) at different rotation speeds (Figure 4c). As shown in the inset, linear fitting of the Koutecky-Levich plot at 0.55 to 0.70 V (see Supplementary Equations) suggests an electron transfer number of 4, which corresponds to a full reduction of O_2 to OH^-. (ref [17, 39]) Figure 4d shows the LSV of Ru/NG and Pt/C in O_2-saturated solution at 900 rpm. The onset ORR potential of Ru/NG is close to that of Pt/C at ~ 0.85 V, and the current density becomes slightly lower at higher overpotentials. These merits make Ru/NG promising for use as a catalyst in various energy conversion applications.

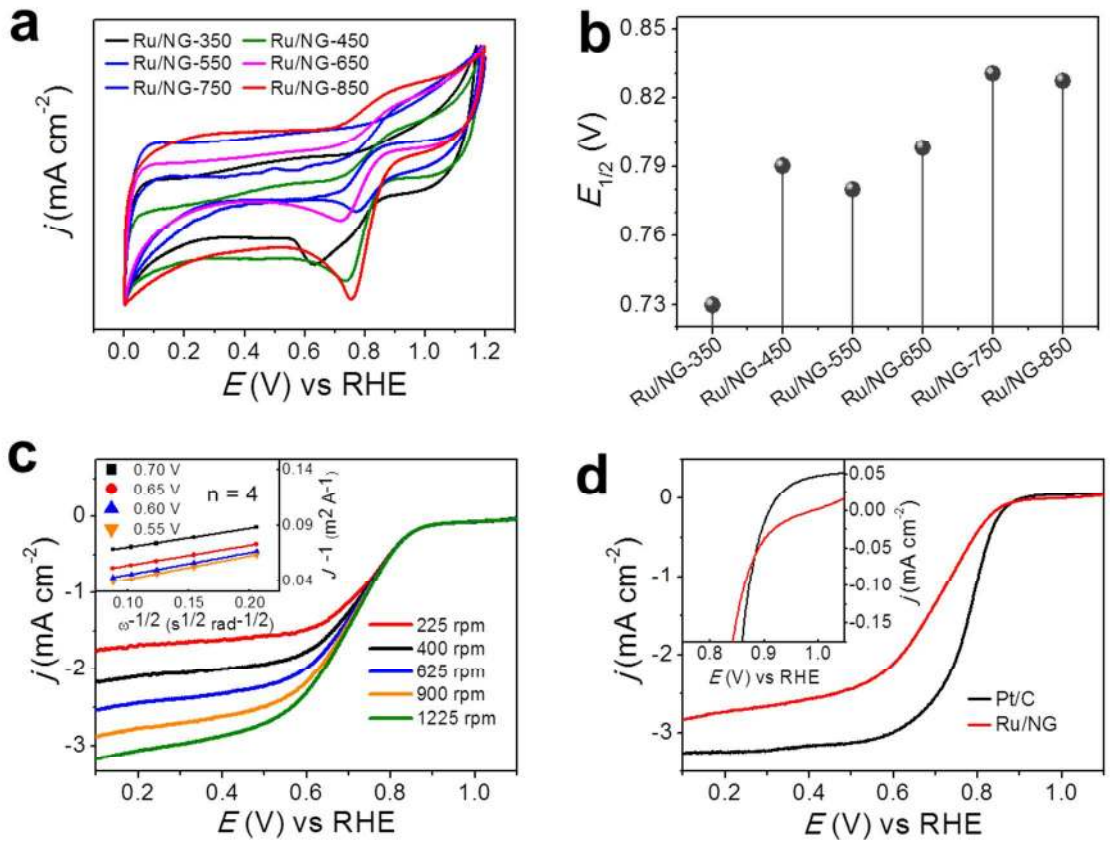

Figure 4. ORR activity of Ru/NG at varying temperatures. (a) CV of Ru/NG in O_2-saturated 0.1 M KOH solution at scan rate of 5 mV s^{-1}. (b) Summary of $E_{1/2}$ of oxygen reduction potential of Ru/NG synthesized at different temperature. (c) Rotating-disk voltammograms of Ru/NG in O_2-saturated 0.1 M KOH solution at different rotating rate. The scan rate is 5 mV s^{-1}. Inset shows

the Koutecky-Levich plot at different potentials and the linear fitting reveals a four-electron oxygen reduction pathway. (d) Comparison of rotating-disk voltammograms of Ru/NG and Pt/C at 900 rpm rotating speed. The inset expands the onset region.

Conclusions

In summary, we have developed a multi-functional crystalline Ru-nanocluster electrocatalyst. The materials exhibit high-performance catalytic activity in HER and ORR. The current density and TOF values of Ru/NG-750 are superior to those of state-of-the-art transition metal dichalcogenide in acid media and even Pt/C in alkaline media. Moreover, Ru/NG can efficiently convert O_2 into OH^- *via* a 4 *e* process at a current density comparable to that in Pt/C, which makes it an excellent candidate for use as a cathode in ORR fuel cells. Noting that price of Ru is only ~1/30 of Pt's (Johnson Matthey), the Ru/NG holds a high promise for various electrocatalysis reactions and represents an important advance towards the development of effective and efficient catalysts for renewable energy conversions.

Acknowledgements

Work at NREL was supported by U.S. DOE under Contract No. DE-AC36-08GO28308, and used computational resources sponsored by the DOE's office of EERE located at NREL. The Air Force Office of Scientific Research (FA9550-14-1-0111) also provided support.

Supporting Information. Additional graphs, images and equations. This can be accessed *via* the Internet free of charge at http://pubs.acs.org.

References

1. Thomas, G. *Overview of Storage Development - Doe Hydrogen Program*; Sandia National Laboratories: 2000.

2. Dehoratiis, G.; Dillich, S.; Randolph, K.; Miller, E.; Sutherland, E.; Peterson, D.; Studer, S.; Soto, H.; Hershkowitz, F.; Holladay, J.; Sing, C.; Rufael, T.; Pakrs, G.; Ruth, M.; Jarvi, T. Hydrogen Production Technical Team Roadmap. *U.S. DRIVE* **2013**, *June*.

3. Kibsgaard, J.; Jaramillo, T. F. Molybdenum Phosphosulfide: An Active, Acid-Stable, Earth-Abundant Catalyst for the Hydrogen Evolution Reaction. *Angew. Chem. Int. Ed.* **2014**, *53*, 14433-14437.

4. Xiao, P.; Sk, M. A.; Thia, L.; Ge, X. M.; Lim, R. J.; Wang, J. Y.; Lim, K. H.; Wang, X. Molybdenum Phosphide as an Efficient Electrocatalyst for the Hydrogen Evolution Reaction. *Energy Environ. Sci.* **2014**, *7*, 2624-2629.

5. Morales-Guio, C. G.; Hu, X. L. Amorphous Molybdenum Sulfides as Hydrogen Evolution Catalysts. *Acc. Chem. Res.* **2014**, *47*, 2671-2681.

6. McCrory, C. C. L.; Jung, S. H.; Peters, J. C.; Jaramillo, T. F. Benchmarking Heterogeneous Electrocatalysts for the Oxygen Evolution Reaction. *J. Am. Chem. Soc.* **2013**, *135*, 16977-16987.

7. Su, H. Y.; Gorlin, Y.; Man, I. C.; Calle-Vallejo, F.; Norskov, J. K.; Jaramillo, T. F.; Rossmeisl, J. Identifying Active Surface Phases for Metal Oxide Electrocatalysts: A Study of Manganese Oxide Bi-Functional Catalysts for Oxygen Reduction and Water Oxidation Catalysis. *Phys. Chem. Chem. Phys.* **2012**, *14*, 14010-14022.

8. Gong, M.; Li, Y. G.; Wang, H. L.; Liang, Y. Y.; Wu, J. Z.; Zhou, J. G.; Wang, J.; Regier, T.; Wei, F.; Dai, H. J. An Advanced Ni-Fe Layered Double Hydroxide Electrocatalyst for Water Oxidation. *J. Am. Chem. Soc.* **2013**, *135*, 8452-8455.

9. Tang, D.; Han, Y. Z.; Ji, W. B.; Qiao, S.; Zhou, X.; Liu, R. H.; Han, X.; Huang, H.; Liu, Y.; Kong, Z. H. A High-Performance Reduced Graphene Oxide/ZnCo Layered Double Hydroxide Electrocatalyst for Efficient Water Oxidation. *Dalton Trans.* **2014**, *43*, 15119-15125.

10. Helm, M. L.; Stewart, M. P.; Bullock, R. M.; DuBois, M. R.; DuBois, D. L. A Synthetic Nickel Electrocatalyst with a Turnover Frequency above 100,000 $S(^{-1})$ for H_2 Production. *Science* **2011**, *333*, 863-866.

11. Tard, C.; Liu, X. M.; Ibrahim, S. K.; Bruschi, M.; De Gioia, L.; Davies, S. C.; Yang, X.; Wang, L. S.; Sawers, G.; Pickett, C. J. Synthesis of the H-Cluster Framework of Iron-Only Hydrogenase. *Nature* **2005**, *433*, 610-613.

12. Liu, Y.; J., W.; Hackenberg, K. P.; Zhang, J.; Wang, Y. M.; Yang, Y.; Keyshar, K.; Gu, J.; Ogitsu, T.; Vajtai, R.; Lou, J.; Ajayan, P. M.; Wood, B. C.; Yakobson, B. I. Self-Optimizing Layered Hydrogen Evolution Catalyst with High Basal-Plane Activity. *arXiv:1608.05755*.

13. Kibsgaard, J.; Jaramillo, T. F.; Besenbacher, F. Building an Appropriate Active-Site Motif into a Hydrogen-Evolution Catalyst with Thiomolybdate $[Mo_3S_{13}]^{(2-)}$ Clusters. *Nature Chem.* **2014**, *6*, 248-253.

14. Xia, J.; Chen, F.; Li, J.; Tao, N. Measurement of the Quantum Capacitance of Graphene. *Nat. Nanotechnol.* **2009**, *4*, 505-509.

15. Chen, G.; Liu, Y.; Liu, F.; Zhang, X. Fabrication of Three-Dimensional Graphene Foam with High Electrical Conductivity and Large Adsorption Capability. *Appl. Surf. Sci.* **2014**, *311*, 808-815.

16. Bolotin, K. I.; Sikes, K. J.; Jiang, Z.; Klima, M.; Fudenberg, G.; Hone, J.; Kim, P.; Stormer, H. L. Ultrahigh Electron Mobility in Suspended Graphene. *Solid State Commun.* **2008**, *146*, 351-355.

17. Liang, Y.; Li, Y.; Wang, H.; Zhou, J.; Wang, J.; Regier, T.; Dai, H. Co_3O_4 Nanocrystals on Graphene as a Synergistic Catalyst for Oxygen Reduction Reaction. *Nat. Mater.* **2011**, *10*, 780-786.

18. Beliatis, M. J.; Gandhi, K. K.; Rozanski, L. J.; Rhodes, R.; McCafferty, L.; Alenezi, M. R.; Alshammari, A. S.; Mills, C. A.; Jayawardena, K. D. G. I.; Henley, S. J.; Silva, S. R. P., Hybrid Graphene-Metal Oxide Solution Processed Electron Transport Layers for Large Area High-Performance Organic Photovoltaics. *Adv. Mater.* **2014**, *26*, 2078-2083.

19. Shin, S. I.; Go, A.; Kim, I. Y.; Lee, J.; Lee, Y.; Hwang, S. J. A Beneficial Role of Exfoliated Layered Metal Oxide Nanosheets in Optimizing the Electrocatalytic Activity and Pore Structure of Pt-Reduced Graphene Oxide Nanocomposites. *Energy Environ. Sci.* **2013**, *6*, 608-617.

20. Kumar, B.; Asadi, M.; Pisasale, D.; Sinha-Ray, S.; Rosen, B. A.; Haasch, R.; Abiade, J.; Yarin, A. L.; Salehi-Khojin, A. Renewable and Metal-Free Carbon Nanofibre Catalysts for Carbon Dioxide Reduction. *Nat. Commun.* **2013**, *4*, 2819.

21. Li, Y.; Wang, H.; Xie, L.; Liang, Y.; Hong, G.; Dai, H. MoS_2 Nanoparticles Grown on Graphene: An Advanced Catalyst for the Hydrogen Evolution Reaction. *J. Am. Chem. Soc.* **2011**, *133*, 7296-7299.

22. Bicelli, L. P. Kinetics of Electrolytic Evolution of Hydrogen in Alkaline Solutions. *Chimica & L Industria* **1973**, *55*, 792-797.

23. Popczun, E. J.; McKone, J. R.; Read, C. G.; Biacchi, A. J.; Wiltrout, A. M.; Lewis, N. S.; Schaak, R. E. Nanostructured Nickel Phosphide as an Electrocatalyst for the Hydrogen Evolution Reaction. *J. Am. Chem. Soc.* **2013**, *135*, 9267-9270.

24. Popczun, E. J.; Read, C. G.; Roske, C. W.; Lewis, N. S.; Schaak, R. E. Highly Active Electrocatalysis of the Hydrogen Evolution Reaction by Cobalt Phosphide Nanoparticles. *Angew. Chem. Int. Ed.* **2014**, *53*, 5427-5430.

25. Voiry, D.; Yamaguchi, H.; Li, J. W.; Silva, R.; Alves, D. C. B.; Fujita, T.; Chen, M. W.; Asefa, T.; Shenoy, V. B.; Eda, G.; Chhowalla, M. Enhanced Catalytic Activity in Strained Chemically Exfoliated WS_2 Nanosheets for Hydrogen Evolution. *Nat. Mater.* **2013**, *12*, 850-855.

26. Ye, R.; del Angel-Vicente, P.; Liu, Y. Y.; Arellano-Jimenez, M. J.; Peng, Z.; Wang, T.; Li, Y.; Yakobson, B. I.; Wei, S.; Yacaman, M. J.; Tour, J. M. High-Performance Hydrogen Evolution from $MoS_{2(1-X)}P_{(X)}$ Solid Solution. *Adv. Mater.* **2016**, *28*, 1427-1432.

27. Groves, M. N.; Chan, A. S. W.; Malardier-Jugroot, C.; Jugroot, M. Improving Platinum Catalyst Binding Energy to Graphene through Nitrogen Doping. *Chem. Phys. Lett.* **2009**, *481*, 214-219.

28. Zhang, L. S.; Liang, X. Q.; Song, W. G.; Wu, Z. Y. Identification of the Nitrogen Species on N-Doped Graphene Layers and Pt/Ng Composite Catalyst for Direct Methanol Fuel Cell. *Phys. Chem. Chem. Phys.* **2010**, *12*, 12055-12059.

29. Jafri, R. I.; Rajalakshmi, N.; Ramaprabhu, S. Nitrogen-Doped Multi-Walled Carbon Nanocoils as Catalyst Support for Oxygen Reduction Reaction in Proton Exchange Membrane Fuel Cell. *J. Power Sources* **2010**, *195*, 8080-8083.

30. Blöchl, P. E. Projector Augmented-Wave Method. *Phys. Rev. B* **1994**, *50*, 17953-17979.

31. Kresse, G.; Joubert, D. From Ultrasoft Pseudopotentials to the Projector Augmented-Wave Method. *Phys. Rev. B* **1999**, *59*, 1758-1775.

32. Perdew, J. P.; Burke, K.; Ernzerhof, M. Generalized Gradient Approximation Made Simple. *Phys. Rev. Lett.* **1996**, *77*, 3865-3868.

33. Kresse, G.; Hafner, J. *Ab Initio* Molecular Dynamics for Liquid Metals. *Phys. Rev. B* **1993**, *47*, 558-561.

34. Kresse, G.; Furthmüller, J. Efficient Iterative Schemes for *Ab Initio* Total-Energy Calculations Using a Plane-Wave Basis Set. *Phys. Rev. B* **1996**, *54*, 11169-11186.

35. Nørskov, J. K.; Bligaard, T.; Logadottir, A.; Kitchin, J. R.; Chen, J. G.; Pandelov, S.; Stimming, U. Trends in the Exchange Current for Hydrogen Evolution. *J. Electrochem. Soc.* **2005**, *152*, J23-J26.

36. Subbaraman, R.; Tripkovic, D.; Chang, K. C.; Strmcnik, D.; Paulikas, A. P.; Hirunsit, P.; Chan, M.; Greeley, J.; Stamenkovic, V.; Markovic, N. M. Trends in Activity for the Water Electrolyser Reactions on 3d M(Ni,Co,Fe,Mn) Hydr(Oxy)Oxide Catalysts. *Nat. Mater.* **2012**, *11*, 550-557.

37. Subbaraman, R.; Tripkovic, D.; Strmcnik, D.; Chang, K. C.; Uchimura, M.; Paulikas, A. P.; Stamenkovic, V.; Markovic, N. M. Enhancing Hydrogen Evolution Activity in Water Splitting by Tailoring Li^{+}-$Ni(OH)_{(2)}$-Pt Interfaces. *Science* **2011**, *334*, 1256-1260.

38. Grimme, S.; Antony, J.; Ehrlich, S.; Krieg, H. A Consistent and Accurate Ab Initio Parametrization of Density Functional Dispersion Correction (Dft-D) for the 94 Elements H-Pu. *J. Chem. Phys.* **2010**, *132*, 154104.

39. Mayrhofer, K. J. J.; Strmcnik, D.; Blizanac, B. B.; Stamenkovic, V.; Arenz, M.; Markovic, N. M. Measurement of Oxygen Reduction Activities *Via* the Rotating Disc Electrode

Method: From Pt Model Surfaces to Carbon-Supported High Surface Area Catalysts. *Electrochim. Acta* **2008**, *53*, 3181-3188.

Table of Contents Graphic